A 2-dimensional Data Detrending Technique for Equatorial Plasma Bubble Studies Using GOLD Far Ultraviolet Observations

Rezy Pradipta[1], Chaosong Huang[2], and Keith M. Groves[1]

Corresponding author: Rezy Pradipta, Institute for Scientific Research, Boston College, 140 Commonwealth Avenue, Chestnut Hill, MA 02467, USA (rezy.pradipta@bc.edu)

[1]Institute for Scientific Research, Boston College, Chestnut Hill, Massachusetts, USA

[2]Air Force Research Laboratory, Kirtland AFB, Albuquerque, New Mexico, USA

Key Points.

- A 2-dimensional data detrending method based on mechanical analogy of rolling a spherical ball on rough and uneven surface is formulated
- The data detrending method may be effective for revealing large-scale equatorial plasma bubble structures in 135.6 nm GOLD observation data
- Enhanced equatorial plasma bubble structures in nighttime GOLD images may be useful for development of more advanced practical applications

Abstract. We formulate a numerical data detrending technique that can be used to help reveal large-scale equatorial plasma bubble (EPB) structures in 2-dimensional data from the Global-scale Observations of the Limb and Disk (GOLD) mission. This GOLD data detrending technique is inspired by and is a generalization of a previous rolling-barrel data detrending method for 1-dimensional total electron content (TEC) observations on individual global positioning system (GPS) satellite passes. This 2-dimensional GOLD data detrending technique treats the observed 135.6 nm radiance as a function of longitude and latitude as an uneven terrain, where EPBs appear as deep but narrow elongated valleys. The unperturbed background radiance is inferred by rolling a ball on the 2-dimensional terrain to skip over the EPB valleys. The two degrees-of-freedom possessed by the rolling ball allow it to smoothly trace the edges of EPB depletions, without falling into the deep valleys. Surface interpolation of radiance values at the ball's contact points onto the whole domain produces the baseline radiance. Subtracting the baseline from the original radiance data yields the net detrended radiance. As a result of the detrending, sharper contrast is present between EPB deple-

tions and the ambient surroundings. As such, this new 2-dimensional GOLD data detrending may potentially open the door to the development of other more advanced techniques for automated EPB detection and tracking, or data assimilation into low-latitude space domain awareness (SDA) information ecosystems.

1. Introduction

In the present paper, we introduce a new numerical data detrending technique that can be applied to the analysis of 2-dimensional nighttime airglow data from the National Aeronautics and Space Administration (NASA) Global-scale Observations of the Limb and Disk (GOLD) mission [e.g. *Eastes et al.*, 2017, 2019, 2020]. The formulation of this GOLD data detrending technique was motivated by the need to reliably identify and track dark bands (depletions) associated with equatorial plasma bubbles (EPBs) in the nighttime GOLD observations [e.g. *Karan et al.*, 2020, 2023; *Martinis et al.*, 2020; *Rodriguez-Zuluaga et al.*, 2021; *Sousasantos et al.*, 2023]. Although the EPB-associated depletions are often already visible in the original GOLD images, a proper data detrending process will make the EPB structures significantly clearer and much more easily identifiable. The main reason for this propensity is the fact that the low-latitude ionosphere is highly inhomogeneous, with two large crests of equatorial ionization anomaly (EIA) at approximately $\pm 15^\circ$ magnetic latitude on either side of the geomagnetic equator line [*Appleton*, 1946; *Rishbeth*, 2000; *Balan et al.*, 2018 and references therein]. This inhomogeneous plasma density configuration causes EPB structures to be highly visible at the EIA crests but much less identifiable anywhere else. For this reason, data detrending can be performed as a part of preliminary data processing in EPB studies [e.g. *Portillo et al.*, 2008; *Seemala and Valladares*, 2011; *Magdaleno et al.*, 2012; *Tang and Chen*, 2022].

For total electron content (TEC) data from global navigation satellite system (GNSS) observations, the data detrending process is usually performed on the TEC time series along individual satellite passes. In order to reveal the TEC depletions associated with

EPBs effectively, here one can use e.g. a special detrending technique described in *Pradipta et al.* [2015] for the TEC data detrending process during each GPS satellite pass. The net detrended ΔTEC is obtained by subtracting the inferred TEC baseline from the original TEC values. The final products in the form of 2-dimensional ΔTEC maps themselves are usually assembled after all the TEC data detrending process along individual GNSS satellite passes have been completed. On the other hand, the situation for the GOLD data is rather different because the observations inherently come in 2-dimensional form. As such, an effective data detrending method with operational principles that equally match the 2-dimensional nature of the GOLD measurements is desired.

In principle, the detrending of GOLD FUV images to reveal EPB-associated depletions can also be performed using the regular 1-dimensional rolling barrel technique [*Pradipta et al.*, 2015], as recently demonstrated by *Adkins and England* [2023]. In the aforementioned work [*Adkins and England*, 2023], GOLD FUV images were first transformed from geographic longitude/latitude (GLON/GLAT) coordinate into quasi-dipole geomagnetic (QDLON/QDLAT) coordinate, and the 1-dimensional rolling-barrel detrending technique was applied consecutively for each QDLAT — one QDLAT slice at a time. A slight drawback may potentially arise in this case because the detrending process for each QDLAT slice is done separately/independently of other QDLAT slices. This slice-by-slice rastering could create a 2-dimensional baseline with slightly "fibrous/filamentous" texture that runs along magnetic east/west orientation, unless some additional smoothing is applied. The new 2-dimensional rolling-ball detrending method is intended to remedy this potential issue. Here, the aforementioned issue would be avoided by the 2 degrees-of-freedom of the rolling ball, which naturally incorporate data points from different LON/LAT slices at once when inferring the baseline.

The following sections below present a systematic description of this proposed GOLD data detrending technique. In Section 2, we describe the basic mathematical formulation and the numerical procedures for this data detrending technique. In Section 3, we provide an illustrative step-by-step working example of this data detrending procedure, and discuss a potential application of the detrended GOLD images produced by the procedure. In Section 4, we present the conclusion.

2. Basic Principles

Figure 1 illustrates the general idea of this new data detrending technique, which is intended for the analysis of nighttime 135.6 nm far ultraviolet (FUV) radiance data from the NASA GOLD mission. As mentioned above, the main goal of this data detrending technique is to help reveal large-scale field-aligned depletions associated with EPBs. This new data detrending technique is a 2-dimensional generalization of a similar rolling-barrel data detrending technique [*Pradipta et al.*, 2015] that operates in 1-dimension only. In the present case, the rolling barrel is replaced with a rolling ball with two degrees of freedom to navigate an uneven 2-dimensional terrain defined by the nighttime NASA GOLD FUV airglow radiance data. Here we describe the underlying mathematical principles behind this new data detrending technique. **Figure 1**

In this data detrending procedure, the GOLD FUV radiance $\mathcal{R}$ (in Rayleighs, R) as a function of latitude Λ and longitude Φ is first transformed via variable scalings. The variable scalings are useful for creating a “terrain” with geometrical features that have comparable scale sizes in all 3 dimensions. In particular, we apply the following set of transformations: x = longitude/Φ_0; y = latitude/Λ_0; and $z = \log_{10}[(\mathcal{R} + g_0)/G_0]$. The most suitable scaling factors (determined by trial-and-error) for this purpose were $\Phi_0 = 12°$, $\Lambda_0 = 5°$, $g_0 = 24$ R + min($\mathcal{R}$), and $G_0 = 0.012$ R. In this xyz-space, the radius of the rolling ball is $R_0 = 1$ by default. This transformation compresses the dynamic range of the "terrain height" (representing the radiance values), and gives us a controlled way to select the effective size of the rolling ball relative to the terrain. It would facilitate the rolling ball to produce good contact points for inferring the baseline level. In the Supplementary Material, we provide an example illustrating different effects between untransformed radiance versus logarithmic transformation for the terrain height z in the detrending process.

In the rolling-barrel detrending, we work with 1-dimensional data (e.g. TEC as a function of time) that is treated as an imaginary terrain/surface for the barrel to roll on. When encountering a valley in the terrain (i.e. depletion or negative excursion in the data), a sufficiently large barrel would be able to skip over the valley. Based on the contact points made between the barrel and the terrain/surface, this mechanical rolling motion enables us to infer a baseline that is unaffected by the presence of such valley(s). In the rolling-ball detrending, we extend the same concept for 2-dimensional case (e.g. radiance as a function of longitude and latitude). Similar to a barrel, a ball is essentially a collection of circular disks/wheels — which makes the extension of this concept possible. In Figure 1, we illustrate the geometrical configuration of such ball (with cross-sectional disks/wheels shown) on a terrain that contains some depletions. A large enough ball will be able to skip over these depletions.

Unlike in the 1-dimensional case of rolling-barrel detrending where only one unique circular disk is involved in the mathematical formulation, in this 2-dimensional case of rolling-ball detrending we are forced to consider not only the central wheel but also the off-center wheel(s). In Figure 1, the central wheel is shown in blue and an off-center wheel in red. This additional consideration is needed because the full mechanics of a rolling ball opens the possibility for different off-center wheel(s) to make contact with the terrain, depending on the chosen direction of the roll and the exact shape of the terrain. In the diagram, the radius of an off-center wheel is denoted as R_1 and the distance of the off-center wheel from the center wheel is denoted as $d_\perp$.

Figure 2 shows a bird's eye view of the situation faced by the rolling ball at any given point while navigating over the terrain. The current contact point of the ball is at $(x_0,\, y_0)$, and the roll direction is at a bearing angle φ. The immediate forward area of the roll (i.e. the "hit zone") is a circle with the same radius as the ball, placed at a forward offset such that the circle is tangential to the pivot axis line. A grid point on the terrain is highlighted as a possible next contact point (i.e. a "hit candidate"). In fact, all the grid points within the immediate forward area are considered in the contact point calculation.

Figure 2

In the xy-coordinate, the equation for the main line of this roll direction (aligned with the central wheel) is given by

$$y = y_0 + \frac{(x - x_0)}{\tan\varphi}. \tag{1}$$

The distance $d_\parallel$ between the pivot axis of the roll and the "hit candidate" is given by the dot product between two vectors $\vec{\mathbf{d}} = [x - x_0,\ y - y_0]$ and $\hat{\mathbf{e}}_r = [\sin\varphi,\ \cos\varphi]$ with the base of these vectors placed at $(x_0,\, y_0)$. The first vector $\vec{\mathbf{d}}$ is pointing from the current contact point to the "hit candidate" point, and the second vector $\hat{\mathbf{e}}_r$ is a unit vector pointing along the forward roll direction. Here, the dot product works because $d_{\|}$ is a sideways projection of $\vec{\mathbf{d}}$ onto the line of forward roll direction. This line projection via dot product operation yields

$$d_{\|} = [x - x_0,\ y - y_0] \cdot [\sin\varphi,\ \cos\varphi] = (x - x_0)\ \sin\varphi + (y - y_0)\ \cos\varphi. \tag{2}$$

In addition, we also have the following identity:

$$d_{\|}^2 + d_{\perp}^2 = (x - x_0)^2 + (y - y_0)^2, \tag{3}$$

as both sides of the equation equal the Euclidean distance (via the Pythagorean theorem) between the current contact point and the "hit candidate" point.

Figure 3

Figure 3 shows a diagram illustrating the basic mechanics that controls the rolling process. At each step in the rolling process, the problem is to determine which point on the terrain will be the next contact point for the ball. This is done by considering a subset of grid points on the terrain within the immediate forward-rolling zone of the ball. For each grid point within this area, we determine the corresponding off-center wheel that could hit the grid point as the ball rolls forward. We then compute the angle $\delta \equiv \beta - \theta$ as depicted in the diagram. The grid point on the terrain with the smallest δ-angle will be the next contact point for the ball.

With a given $d_{\perp}$, the radius R_0 of the central wheel and the radius R_1 of the off-center wheel are related via $R_0^2 = R_1^2 + d_{\perp}^2$ based on the Pythagorean theorem. It means that the relation $R_1 = \sqrt{R_0^2 - d_{\perp}^2}$ holds. Here, the pivot point is at a coordinate $(x_0,\, y_0,\, z_0)$ and the candidate for next contact point is at a coordinate $(x,\, y,\, z)$. For convenience, we may also define a set of increments to relate the two coordinates via $x = x_0 + \Delta x$, $y = y_0 + \Delta y$, and $z = z_0 + \Delta z$.

Of main interest to us is the angle $\delta \equiv \beta - \theta$, as mentioned previously. The expression for the angle θ is quite straightforward to find, which is given by

$$\tan\theta = \frac{\Delta z}{d_\parallel} = \frac{\Delta z}{\Delta x \, \sin\varphi + \Delta y \, \cos\varphi}. \tag{4}$$

Meanwhile, the expression for the angle β requires more effort to find. Here it is useful to consider a triangle connecting the pivot axis of the roll, the ball's main axis $\mathcal{Q}$, and the point $\mathcal{H}$ on the leading edge that would land the hit. This special triangle is shown in the inset of Figure 3.

With γ defined as the complementary angle of β (i.e. $\gamma + \beta = 90°$), we can apply the cosine rule in order to obtain $R_1^2 = R_0^2 + s^2 - 2R_0\, s \cos\gamma = R_0^2 + s^2 - 2R_0\, s \sin\beta$. Hence, the angle β can be expressed as

$$\sin\beta = \frac{s^2 + R_0^2 - R_1^2}{2R_0\, s}. \tag{5}$$

Using the known geometrical relations $s^2 = d_\parallel^2 + \Delta z^2$ and $R_1 = \sqrt{R_0^2 - d_\perp^2}$ (both come from the Pythagorean theorem), we can make some more simplification:

$$\sin\beta = \frac{d_\parallel^2 + \Delta z^2 + R_0^2 - (R_0^2 - d_\perp^2)}{2R_0\sqrt{d_\parallel^2 + \Delta z^2}} = \frac{(d_\parallel^2 + d_\perp^2) + \Delta z^2}{2R_0\sqrt{d_\parallel^2 + \Delta z^2}}. \tag{6}$$

Making use of the identity $d_\parallel^2 + d_\perp^2 = (x - x_0)^2 + (y - y_0)^2 = \Delta x^2 + \Delta y^2$ (cf. Equation 3) and the expression $d_\parallel = (x - x_0)\, \sin\varphi + (y - y_0)\, \cos\varphi$, we can further modify the expression for β to yield

$$\sin\beta = \frac{\Delta x^2 + \Delta y^2 + \Delta z^2}{2R_0\sqrt{(\Delta x \, \sin\varphi + \Delta y \, \cos\varphi)^2 + \Delta z^2}}. \tag{7}$$

Hence the complete expression for the angle $\delta \equiv \beta - \theta$ is given by

$$\delta = \sin^{-1}\left[\frac{\Delta x^2 + \Delta y^2 + \Delta z^2}{2R_0\sqrt{(\Delta x \, \sin\varphi + \Delta y \, \cos\varphi)^2 + \Delta z^2}}\right] - \tan^{-1}\left[\frac{\Delta z}{\Delta x \, \sin\varphi + \Delta y \, \cos\varphi}\right]. \tag{8}$$

For all the terrain points located within the ball's immediate forward-rolling zone, we must find one with the smallest δ-angle in order to determine the next contact point for the rolling ball.

Using the aforementioned basic mechanics, we will roll the ball around the whole terrain in xy-space and mark the contact points. We will then take the radiance values at the contact points and interpolate them onto the entire terrain grid. This interpolation will establish the baseline radiance level that excludes the EPB depletions — i.e. an essentially "depletion-free" baseline radiance. Subtracting this baseline from the original data will give us the net radiance values and reveal the EPB depletions with greater clarity.

3. Illustrative Examples

Figure 4

Figure 4 shows a working example of this data detrending process. Figure 4a shows the original 135.6 nm GOLD FUV radiance data (in geographic latitude/longitude coordinate) from observations made on 2 February 2022 at 21:40 UTC. The dynamic range of the observed radiance value is generally between 0 R and 100 R, with higher radiance values coming from the crests of the equatorial ionization anomaly (EIA). The EIA crests may also exhibit some variations that are recognizable in the GOLD FUV data [*Eastes et al.*, 2023]. A number of EPB-related depletions are already visible in the data, and EPB analysis could be performed with these original GOLD images [e.g. *Aa et al.*, 2020]. However, these depletions can be enhanced further by the data detrending. Figure 4b shows the result of rastering process by the rolling ball as it navigates around the terrain in the xy-space. White circle indicates the size of the ball, and magenta dots mark the ball's contact points. The rastering process begins at the highest point on the terrain, and we start rolling the ball toward a randomly selected direction at an initial bearing angle $\varphi = \varphi_0$. After each roll, we vary the bearing angle φ by a random variable uniformly distributed between $\pm\Delta\varphi$. The magnitude of this "scattering amplitude" is initially set to be quite small at $\Delta\varphi = 20°$, which remains constant while the number of executed rolls are still below 20% of the total number of grid points in the terrain. After that, we progressively increase the magnitude of $\Delta\varphi$ by an additional 10° when the number of executed rolls reach 20%, 40%, 60%, and 80% of the total number of grid points in the terrain, respectively. This randomized "scatter-after-each-roll" policy is intended to prevent the ball from being accidentally trapped in a closed loop. When the ball arrives at the outer boundary, it will be turned back toward the interior of the computational domain, at a new randomly selected bearing angle. The rastering process ends when the number of executed rolls reach the total number of grid points in the terrain. A few additional plots illustrating more details on the progression of the rolling-ball rastering process are provided in the Supplementary Material. In general, there is freedom to implement different strategies for rolling the ball across the terrain.

Figure 4c depicts the 2-dimensional baseline radiance level, obtained by interpolating the radiance values at the contact points onto the whole terrain grid (in regular geographic latitude/longitude coordinate). A bilinear numerical interpolation was used for computing the baseline radiance level. Higher background radiance values are naturally found at the two EIA crests, consistent with the $\sim n_e^2$ dependence of the 135.6 nm OI volume emission rate from ionospheric F-region altitudes, where n_e is the electron density [*Tinsley and Bittencourt*, 1975; *Melendez-Alvira et al.*, 1999; *Qin et al.*, 2015]. Finally, Figure 4d shows the 2-dimensional net radiance profile that was obtained by subtracting the inferred baseline level from the original radiance data (expressed in geographic latitude/longitude coordinate). The typical dynamic range of the net detrended radiance value is between -40 R and 4 R, with deeper depletions generally occurring around the EIA crest locations. In the net radiance data, sharper contrast is present between EPB-associated depletions and the unperturbed regions. This enhanced contrast may help significantly in terms of EPB detection, either visually or computationally, compared to working directly with the original radiance data.

The depth of the elongated depletions in detrended GOLD images may be used to quantify the intensity of EPBs. This concept is aligned with an analysis conducted by *Aa et al.* [2023], in which the differential radiance $\Delta\mathcal{R}$ was obtained by subtracting a running average baseline. The standard deviation of normalized $\Delta\mathcal{R}$ was then used as a Bubble Index to quantify the EPB intensity. In the future, the same could be tried with $\Delta\mathcal{R}$ obtained using the present rolling-ball detrending technique, which may offer some improvement since the EPBs would be more accurately manifested as depletions (i.e. negative excursions) in $\Delta\mathcal{R}$ rather than large-amplitude oscillatory signals (with both hills and valleys).

Other, more advanced applications may also be developed based on the enhanced EPB features observed in the net detrended GOLD FUV images. An example of such application is a 3-dimensional volumetric representation of the large-scale EPB structures. Here we provide a basic conceptual illustration of this particular potential usage of the net detrended GOLD FUV images.

Figure 5 shows a case example to illustrate this potential application. Figure 5a displays a detrended GOLD image on 2 February 2022 at 00:22 UTC, which shows a sequence of large-scale EPB depletion structures between 80°W-20°W longitude. Enhanced by the data detrending process, some branching/bifurcations are also revealed at the tips of these EPB structures. Figure 5b displays the same detrended GOLD image, but with the skeletons/spines of the observed EPB structures added as green line segments on the image. For the purpose of this illustrative example, these EPB spines were determined by manually profiling the observed EPB structures in the detrended GOLD image. In the future, automated profiling of complex EPB spines might potentially be achievable through computational algorithm(s). The profiled EPB spines will be a key ingredient for assembling the 3-dimensional volumetric representation.

Figure 5c shows a visualization plot containing two planar projections of the EPB structures, one along a horizontal plane at 300 km altitude (nominally taken as the 135.6 nm OI emission source height) and the other along a vertical E/W plane at 5°S latitude. Magenta dots at $z = 0$ km are the shadow of the EPB plume structures projected onto ground level. For visualization purposes, we assume that the plasma density is fully depleted at the spine lines. In the neighborhood of each spine line, the depletion is set to subside as a function of distance following a bivariate Gaussian profile with a standard deviation of $\sigma = 0.25°$ in latitude/longitude. In the far-field away from any spine line, there is practically no depletion in plasma density. The simplified depletion profiles were subsequently projected along the geomagnetic field lines using the International Geomagnetic Reference Field (IGRF) model [*Thebault et al.*, 2015; *Alken et al.*, 2021]. On the two planar projections, the relative plasma density values (Rel. N_e) are indicated with colormap.

Figure 5d shows a similar visualization plot, this time displaying a 3-dimensional volumetric representation of the observed EPB structures. Here, the 3-dimensional morphology of the EPBs (which resemble a series of arches) is represented using isosurface at Rel. $N_e = 0.6$ level. The alpha color transparency was set at 0.15 to make the isosurfaces translucent. The depleted part of ionospheric plasma is essentially the volume contained within the arches. The arches are elongated roughly along the N/S direction, turned slightly sideways following the magnetic declination angle. Like in Figure 5c, magenta dots at $z = 0$ km are the shadow of these arches projected onto ground level. This volumetric representation illustrates how the EPB-associated magnetic flux tubes occupy the 3-dimensional space.

Animations that provide additional perspectives on the visualization shown in Figure 5d, viewing the 3-dimensional volumetric structures dynamically from different angles, are included in the Supplementary Material.

For a more comprehensive data assimilation, similar concept can be applied but a few aspects need to be modified. Aspects that would be subject to modifications are as follows. (1) The numerical value of relative depletions at the spine lines will have to be determined empirically from the net radiance and baseline radiance data arrays. (2) The process will no longer be only about the relative level of depletions, but the end result is going to be expressed in terms of ionospheric plasma density and/or TEC values. (3) The background plasma density and/or TEC may be obtained from ionosphere models such as IRI, NeQuick, NET, TIE-GCM, or WAM-IPE [*Coisson et al.*, 2006; *Nava et al.*, 2008; *Quan et al.*, 2014; *Bilitza et al.*, 2022; *Fang et al.*, 2018; *Smirnov et al.*, 2023]. Aside from these few modifications, the process would be quite straightforward: the relative depletion profile is going to be stamped onto the smooth background plasma density and/or TEC profile. This procedure will produce a model ionosphere that contains a representation of the EPB plume structures.

In the conceptual example discussed above, the 3-dimensional volumetric representation of EPB structures may potentially have its practical usage in the context of space situational awareness (SSA) and space domain awareness (SDA) information ecosystems. This potential usage might be directed toward actual implementation if the SSA/SDA system has a focus on low-latitude regions, and concerns not only the physical survivability of space assets in orbit but also their state of radio connectivity in VHF/UHF bands to various terrestrial components [e.g. *Bishop et al.*, 2004; *Belehaki et al.*, 2015; *Mendillo et al.*, 2018; *Bahar et al.*, 2022].

4. Conclusion

We have formulated a new 2-dimensional data detrending method that can be used in the analysis of nighttime GOLD FUV emission data to help reveal large-scale EPB structures. A generalization of a previous GPS TEC data detrending technique in 1-dimension [*Pradipta et al.*, 2015], this new GOLD data detrending method works by a mechanical analogy of rolling a spherical ball on an uneven terrain surface. The rolling ball's ability to skip over EPB-associated depletions (deep-but-narrow valleys in the terrain surface) allows the data detrending method to deduce suitable baseline level to exclude the EPBs. The detrending process enhances the contrast between EPB depletions and the ambient surroundings, making the detrended GOLD images a powerful resource for those conducting EPB research in the South American and Atlantic sectors.

Another objective carried by the proposed GOLD FUV data detrending method is to enable and/or facilitate the development of other, more advanced applications. We have discussed a conceptual example of such potential applications, involving 3-dimensional volumetric representation of EPB structures over a wide range of longitudes. The given example highlights the potential utility of assimilating detrended GOLD FUV images into SSA/SDA information ecosystems. Future work will be directed toward exploring other potential applications of the 2-dimensional GOLD data detrending method. It is hoped that many practical applications using detrended GOLD images (or airglow images more generally) can be realized in the future.

5. Open Research

The NASA GOLD Level 1C observation datafiles for this study are available from the GOLD mission webpage at `https://gold.cs.ucf.edu/data/` or from the NASA Space Physics Data Facility webpage at `https://spdf.gsfc.nasa.gov/pub/data/gold/level1c/`.

Acknowledgments. This work was supported by the NASA GOLD-ICON Guest Investigators (GIGI) program under grant #NNH22OB17A.

Disclaimer: The views expressed are those of the authors and do not necessarily reflect the official policy or position of the Department of the Air Force, the Department of Defense, or the U.S. government.

References

Aa, E., Zou, S., Eastes, R., Karan, D. K., Zhang, S.-R., Erickson, P. J., and Coster, A. J. (2020), Coordinated ground-based and space-based observations of equatorial plasma bubbles, *Journal of Geophysical Research: Space Physics*, 125, e2019JA027569, https://doi.org/10.1029/2019JA027569.

Aa, E., Zhang, S.-R., Liu, G., Eastes, R. W., Wang, W., Karan, D. K., et al. (2023), Statistical analysis of equatorial plasma bubbles climatology and multi-day periodicity using GOLD observations, *Geophysical Research Letters*, 50, e2023GL103510, https://doi.org/10.1029/2023GL103510.

Adkins, V. J., and England, S. L. (2023), Automated detection and tracking of equatorial plasma bubbles utilizing Global-Scale Observations of the Limb and Disk (GOLD) 135.6 nm Data, *Earth and Space Science*, 10, e2023EA002935, https://doi.org/10.1029/2023EA002935.

Alken, P., Thebault, E., Beggan, C. D., et al. (2021), International Geomagnetic Reference Field: the thirteenth generation, *Earth Planets Space*, 73, 49, https://doi.org/10.1186/s40623-020-01288-x.

Appleton, E. V. (1946), Two anomalies in the ionosphere, *Nature*, 157, 691, https://doi.org/10.1038/157691a0.

Bahar, A., Dear, V., Husin, A., Faturahman, A., Harjosuwito, J., and Pradipta, R. (2022), Exploring an Extension of Space Situational Awareness in Southeast Asian Region Utilizing EAR Observation Data, In: Yulihastin, E., Abadi, P., Sitompul, P., Harjupa, W. (eds), Proceedings of the International Conference on Radioscience, Equatorial Atmospheric Science and Environment and Humanosphere Science (INCREASE) 2021, *Springer Proceedings in Physics*, vol 275, Springer, Singapore, https://doi.org/10.1007/978-981-19-0308-3_21.

Balan, N., Liu, L. and Le, H. (2018), A brief review of equatorial ionization anomaly and ionospheric irregularities, *Earth and Planetary Physics*, 2: 257-275, https://doi.org/10.26464/epp2018025.

Belehaki, A., Tsagouri, I., Kutiev, I., Marinov, P., Zolesi, B., Pietrella, M., Themelis, K., Elias, P., and Tziotziou, K. (2015), The European Ionosonde Service: nowcasting and forecasting ionospheric conditions over Europe for the ESA Space Situational Awareness services, *J. Space Weather Space Clim.*, 5, A25, https://doi.org/10.1051/swsc/2015026.

Bilitza, D., Pezzopane, M., Truhlik, V., Altadill, D., Reinisch, B. W., and Pignalberi, A. (2022), The International Reference Ionosphere model: A review and description of an ionospheric benchmark, *Reviews of Geophysics*, 60, e2022RG000792, https://doi.org/10.1029/2022RG000792.

Bishop, G., Bullett, T. W., Groves, K. M., Quigley, S., Doherty, P. H., Sexton, E., Scro, K., Wilkes, R., and Citrone, P. (2004), Operational Space Environment Network Display (OpSEND), *Radio Sci.*, 39, RS1S26, https://doi.org/10.1029/2002RS002836.

Coisson, P., S. M. Radicella, R. Leitinger, and B. Nava (2006), Topside electron density in IRI and NeQuick: Features and limitations, *Adv. Space Res.*, 37(5), 937-942, https://doi.org/10.1016/j.asr.2005.09.015.

Eastes, R. W., McClintock, W. E., Burns, A. G., Anderson, D. N., Andersson, L., Codrescu, M., Correira, J. T., Daniell, R. E., England, S. L., Evans, J. S., Harvey, J., Krywonos, A., Lumpe, J. D., Richmond, A. D., Rusch, D. W., Siegmund, O., Solomon, S. C., Strickland, D. J., Woods, T. N., Aksnes, A., Budzien, S. A., Dymond, K. F., Eparvier, F. G., Martinis, C. R., and Oberheide, J. (2017), The Global-scale Observations of the Limb and Disk (GOLD) mission, *Space Science Reviews*, 212(1-2), 383-408, https://doi.org/10.1007/s11214-017-0392-2.

Eastes, R. W., Solomon, S. C., Daniell, R. E., Anderson, D. N., Burns, A. G., England, S. L., et al. (2019), Global-scale observations of the equatorial ionization anomaly, *Geophysical Research Letters*, 46, 9318-9326, https://doi.org/10.1029/2019GL084199.

Eastes, R. W., McClintock, W. E., Burns, A. G., Anderson, D. N., Andersson, L., Aryal, S., et al. (2020), Initial observations by the GOLD mission, *Journal of Geophysical Research: Space Physics*, 125, e2020JA027823, https://doi.org/10.1029/2020JA027823.

Eastes, R. W., Karan, D. K., Martinis, C., Daniell, R. E., Gan, Q., Burns, A. G., and McClintock, W. E. (2023), GOLD observations of longitudinal variations in the nighttime equatorial ionization anomaly (EIA) crests' latitudes, *Journal of Geophysical Research: Space Physics*, 128, e2022JA031007, https://doi.org/10.1029/2022JA031007.

Fang, T.-W., Fuller-Rowell, T., Yudin, V., Matsuo, T., and Viereck, R. (2018), Quantifying the sources of ionosphere day-to-day variability, *Journal of Geophysical Research: Space Physics*, 123, 9682-9696, https://doi.org/10.1029/2018JA025525.

Karan, D. K., Daniell, R. E., England, S. L., Martinis, C. R., Eastes, R. W., Burns, A. G., and McClintock, W. E. (2020), First zonal drift velocity measurement of equatorial plasma bubbles (EPBs) from a geostationary orbit using GOLD data, *Journal of Geophysical Research: Space Physics*, 125, e2020JA028173, https://doi.org/10.1029/2020JA028173.

Karan, D. K., Eastes, R. W., Daniell, R. E., Martinis, C. R., and McClintock, W. E. (2023), GOLD mission's observation about the geomagnetic storm effects on the nighttime equatorial ionization anomaly (EIA) and equatorial plasma bubbles (EPB) during a solar minimum equinox, *Space Weather*, 21, e2022SW003321, https://doi.org/10.1029/2022SW003321.

Magdaleno, S., Herraiz, M., and Radicella, S. M. (2012), Ionospheric bubble seeker: A java application to detect and characterize ionospheric plasma depletion from

GPS data, *IEEE Transactions on Geoscience and Remote Sensing*, 50(5), 1719-1727, https://doi.org/10.1109/TGRS.2011.216896.

Martinis, C., Daniell, R., Eastes, R., Norrell, J., Smith, J., Klenzing, J., et al. (2021), Longitudinal variation of postsunset plasma depletions from the global-scale observations of the limb and disk (GOLD) mission, *Journal of Geophysical Research: Space Physics*, 126, e2020JA028510, https://doi.org/10.1029/2020JA028510.

Melendez-Alvira, D. J., Meier, R. R., Picone, J. M., Feldman, P. D., and McLaughlin, B. M. (1999), Analysis of the oxygen nightglow measured by the Hopkins Ultraviolet Telescope: Implications for ionospheric partial radiative recombination rate coefficients, *J. Geophys. Res.*, 104(A7), 14901-14913, https://doi.org/10.1029/1999JA900136.

Mendillo, M., Hickey, D., Martinis, C., Wroten, J., and Baumgardner, J. (2018), Space weather nowcasting for area-denied locations: Testing all-sky imaging applications at geomagnetic conjugate points, *Space Weather*, 16, 47-56, https://doi.org/10.1002/2017SW001741.

Nava, B., P. Coisson, and S. M. Radicella (2008), A new version of the NeQuick ionosphere electron density model, *J. Atmos. Sol. Terr. Phys.*, 70(15), 1856-1862.

Portillo, A., Herraiz, M., Radicella, S. M., and Ciraolo, L. (2008), Equatorial plasma bubbles studied using African slant total electron content observations, *Journal of Atmospheric and Solar-Terrestrial Physics*, 70(6), 907-917, https://doi.org/10.1016/j.jastp.2007.05.019.

Pradipta, R., Valladares, C. E., and Doherty, P. H. (2015), An effective TEC data detrending method for the study of equatorial plasma bubbles and traveling ionospheric disturbances, *J. Geophys. Res. Space Physics*, 120, 11,048-11,055, https://doi.org/10.1002/2015JA021723.

Qin, J., Makela, J. J., Kamalabadi, F., and Meier, R. R. (2015), Radiative transfer modeling of the OI 135.6 nm emission in the nighttime ionosphere, *J. Geophys. Res. Space Physics*, 120, 10116-10135, https://doi.org/10.1002/2015JA021687.

Qian, L., Burns, A.G., Emery, B.A., Foster, B., Lu, G., Maute, A., Richmond, A.D., Roble, R.G., Solomon, S.C. and Wang, W. (2014), The NCAR TIE-GCM: A Community Model of the Coupled Thermosphere/Ionosphere System, In *Modeling the Ionosphere-Thermosphere System* (eds J. Huba, R. Schunk and G. Khazanov), https://doi.org/10.1002/9781118704417.ch7.

Rishbeth, H. (2000), The equatorial F-layer: Progress and puzzles, *Ann. Geophys.*, 18, 730, https://doi.org/10.1007/s00585-000-0730-6.

Rodriguez-Zuluaga, J., Stolle, C., Yamazaki, Y., Xiong, C., and England, S. L. (2021), A synoptic-scale wavelike structure in the nighttime equatorial ionization anomaly, *Earth and Space Science*, 8, e2020EA001529, https://doi.org/10.1029/2020EA001529.

Seemala, G. K., and Valladares, C. E. (2011), Statistics of total electron content depletions observed over the South American continent for the year 2008, *Radio Sci.*, 46, RS5019, https://doi.org/10.1029/2011RS004722.

Smirnov, A., Shprits, Y., Prol, F. et al. (2023), A novel neural network model of Earth's topside ionosphere, *Sci Rep*, 13, 1303, https://doi.org/10.1038/s41598-023-28034-z.

Sousasantos, J., Gomez Socola, J., Rodrigues, F.S., et al. (2023), Severe L-band scintillation over low-to-mid latitudes caused by an extreme equatorial plasma bubble: joint observations from ground-based monitors and GOLD, *Earth Planets Space*, 75, 41, https://doi.org/10.1186/s40623-023-01797-5.

Tang, L., and Chen, G. (2022), Equatorial plasma bubble detection using vertical TEC from altimetry satellite, *Space Weather*, 20, e2022SW003142, https://doi.org/10.1029/2022SW003142.

Thebault, E., Finlay, C. C., Beggan, C. D., et al. (2015), International Geomagnetic Reference Field: the 12th generation, *Earth Planet Sp*, 67, 79, https://doi.org/10.1186/s40623-015-0228-9.

Tinsley, B. A., and Bittencourt, J. A. (1975), Determination of F region height and peak electron density at night using airglow emissions from atomic oxygen, *J. Geophys. Res.*, 80(16), 2333-2337, https://doi.org/10.1029/JA080i016p02333.

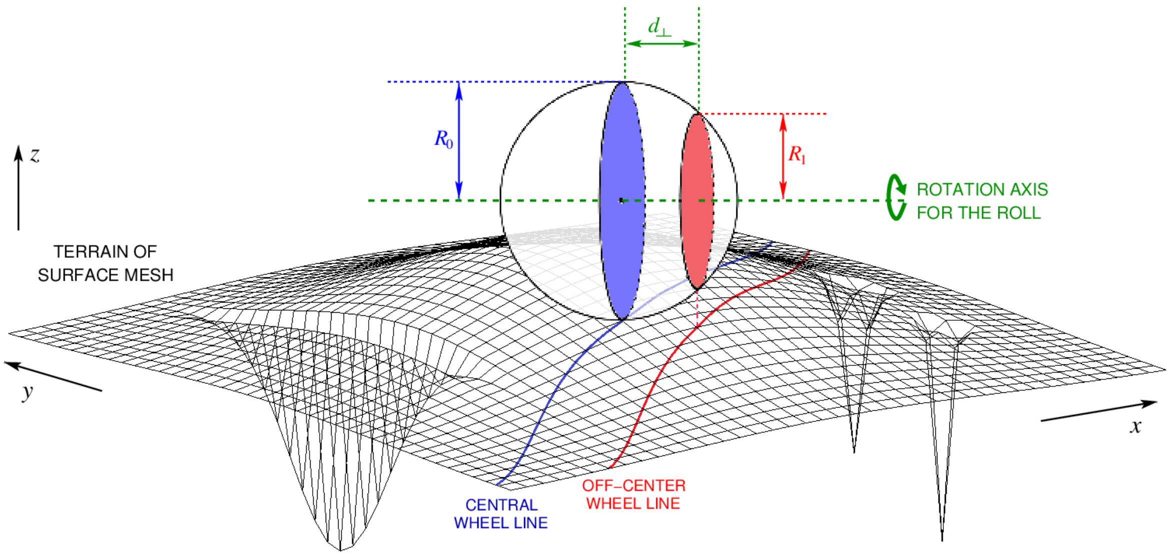

Figure 1. Graphical illustration of 2-dimensional data detrending process using mechanical analogy of a rolling ball on an uneven terrain. A ball with sufficiently large radius should be able to skip/roll over deep-but-narrow valleys, which correspond to EPB depletions in the case of GOLD FUV data.

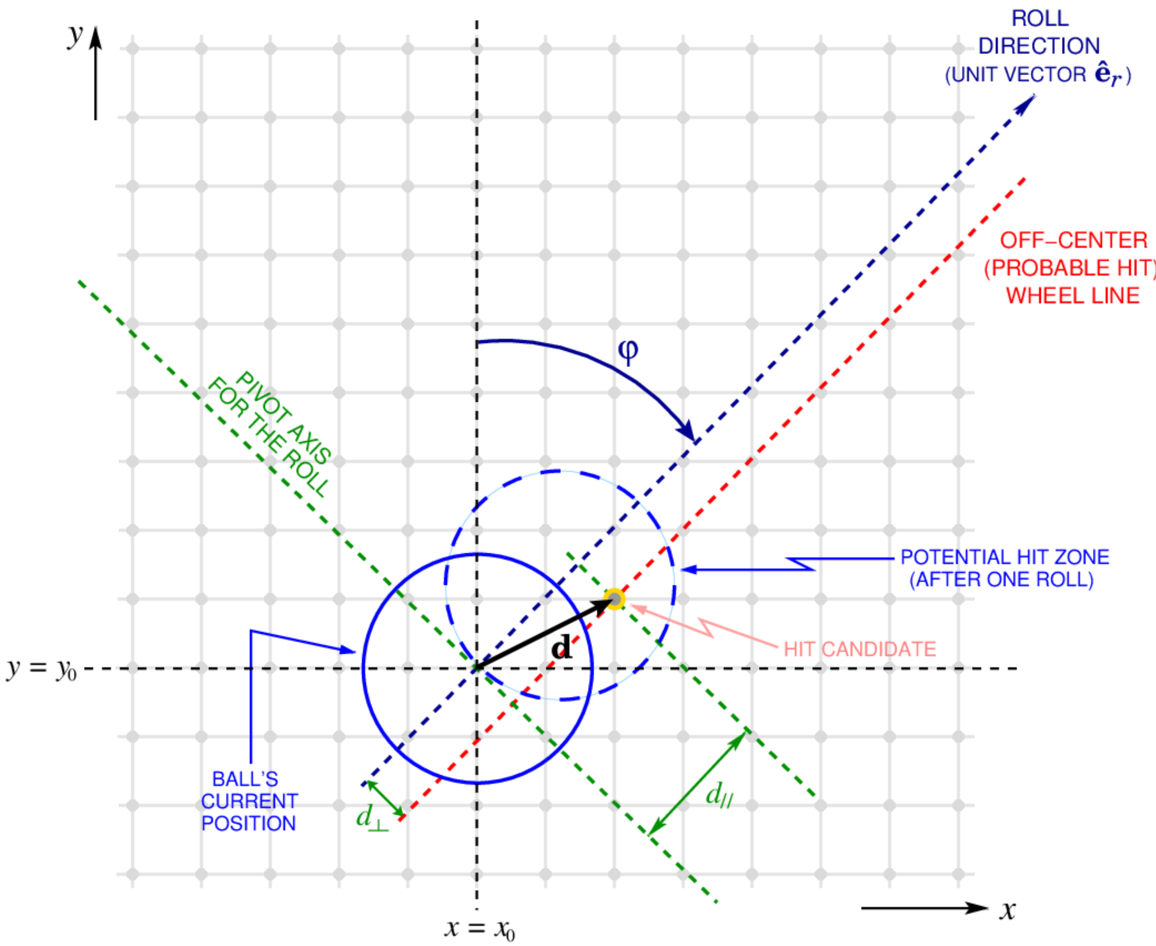

Figure 2. Bird's eye view of the rolling ball on the terrain grid, showing the starting position of the ball (solid circle), the chosen roll direction (at bearing angle φ relative to the y-axis), and the potential hit zone (dashed circle) where one of the grid points would make contact with the ball next. The displacement vector $\vec{\mathbf{d}}$ denotes the relative position of a "hit candidate" from the current contact point $(x_0,\, y_0)$. The roll direction is associated with the unit vector $\hat{\mathbf{e}}_r = [\sin\varphi,\ \cos\varphi]$.

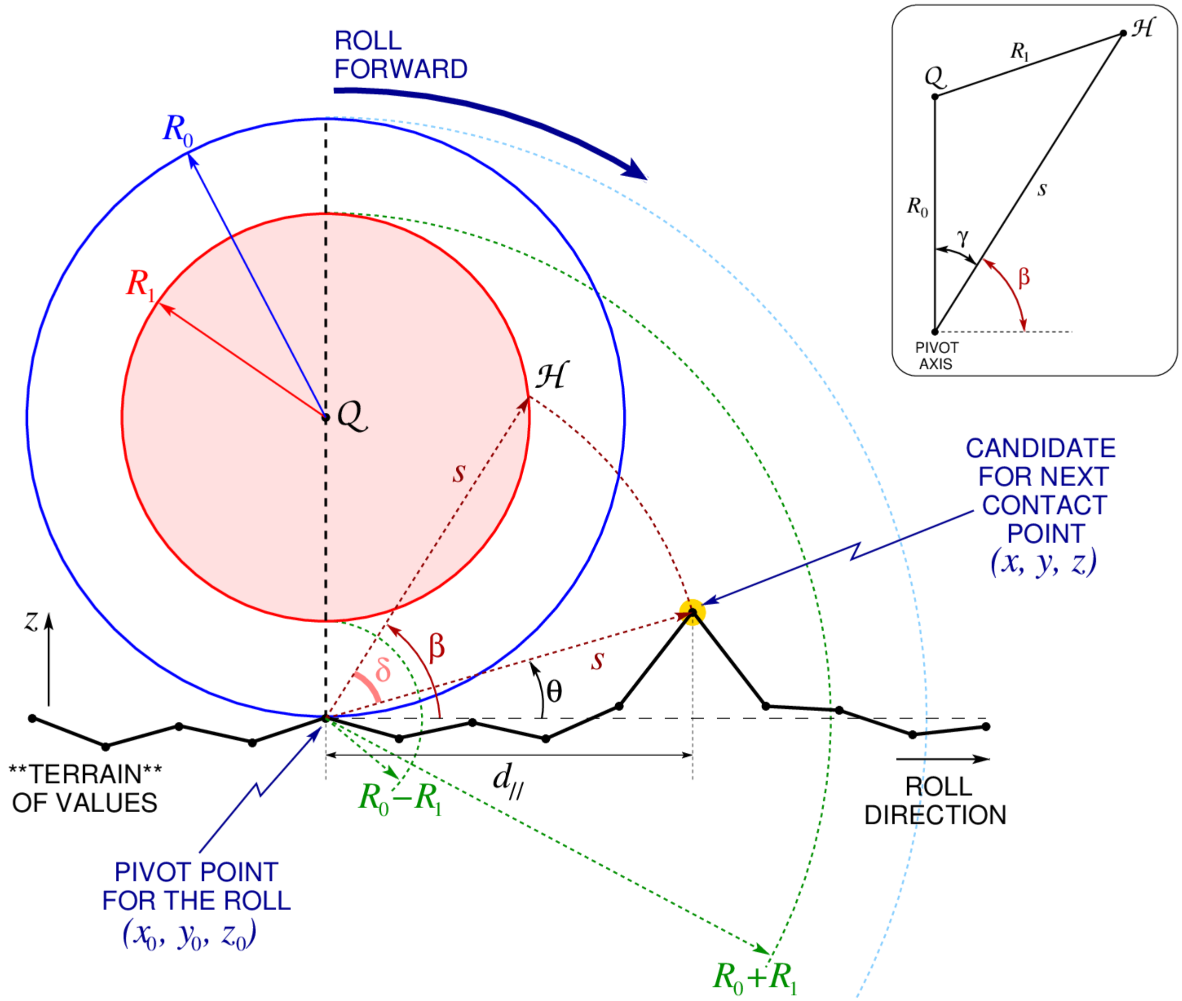

Figure 3. Detailed cross-sectional sideways view of the rolling ball, with one of the grid points on the terrain under focus as a contact candidate. The corresponding off-center wheel (shaded circle) in alignment with the said grid point is shown, where potential contact may happen at the point marked $\mathcal{H}$. Determining the next contact point of the rolling ball is equivalent to finding the grid point with the smallest δ-angle to its corresponding wheel.

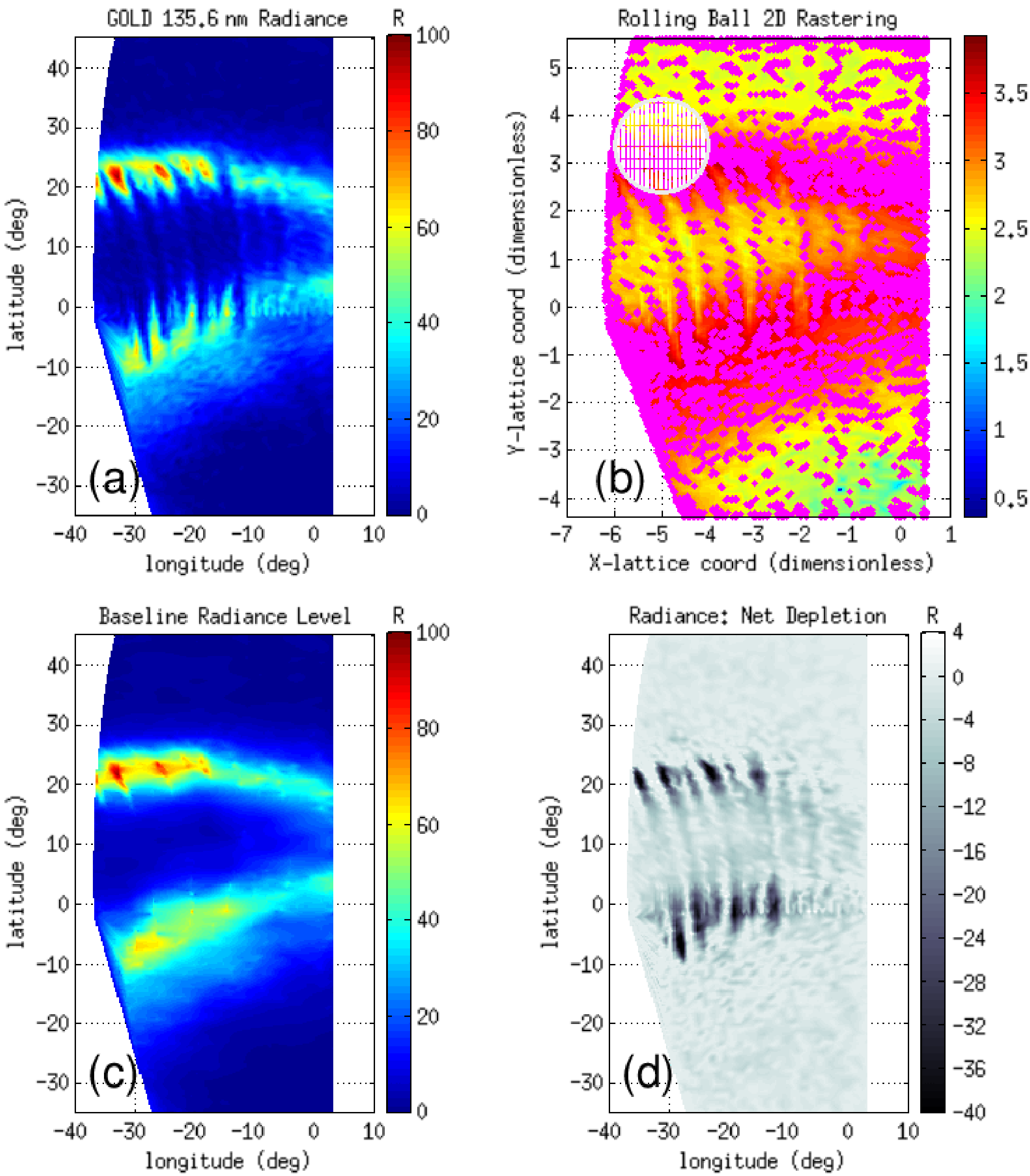

Figure 4. Step-by-step working illustration of the data detrending procedure. (a) Original GOLD radiance data. (b) Navigation/rastering process by the rolling ball over the proverbial terrain. (c) Baseline level obtained by interpolating radiance values at the contact points onto the whole grid. (d) Net radiance values obtained by subtracting the baseline from the original GOLD data.

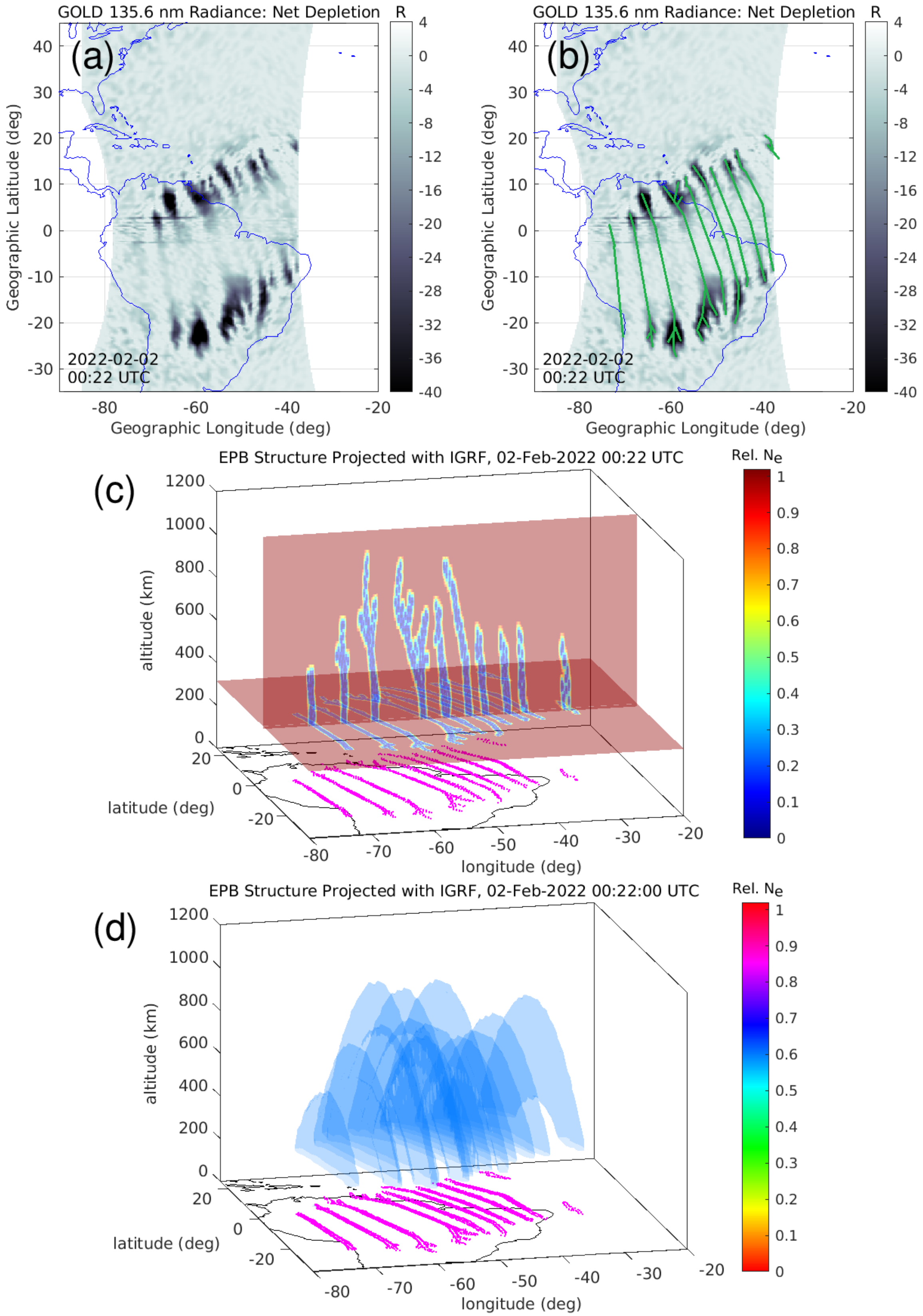

Figure 5. (a) Detrended GOLD image on 2 February 2022 at 00:22 UTC, showing several large-scale EPB structures. (b) The same GOLD image with skeletons/spines of the EPB structures profiled. (c) Horizontal and vertical planar projections of the observed EPB structures using IGRF. (d) A 3-dimensional volumetric representation of the observed EPB structures using IGRF.